



Cite this: *Phys. Chem. Chem. Phys.*,
2021, 23, 18990

Structure and solvation dynamics of the hydroxide ion in ice-like water clusters: a CCSD(T) and car–parrinello molecular dynamics study†

Kono H. Lemke 

Using MP2, CCSD(T) electronic structure theory and *ab initio* molecular dynamics simulations, we explore the structure, solvation dynamics and vibrational spectra of $\text{OH}^-(\text{H}_2\text{O})_n$ clusters. Our study reports new cubic and fused cubic global minima structures of $\text{OH}^-(\text{H}_2\text{O})_n$ for $n = 8–26$ with surface and interior solvation arrangements. In the case of $\text{OH}^-(\text{H}_2\text{O})_{26}$, we show that MP2 and CCSD(T) calculations predict global minima structures with the hydroxide ion occupying the interior region of a densely packed cubic cluster that is secured by ionic hydrogen bonds. More importantly, results from *ab initio* molecular dynamics simulations of $\text{OH}^-(\text{H}_2\text{O})_{26}$ demonstrate that the hydroxide ion remains in the cluster interior and hexa-coordinated, irrespective of the temperature, up to around 175 K, then incrementally transitions from a surface-exposed penta- (170–200 K), to a tetra- (225 K) to a tri-coordinated $\text{OH}^-(\text{H}_2\text{O})_3$ structure at 300 K. Building on our temperature-dependent vibrational power spectra, we are also able to disentangle structure and temperature effects on individual spectral contributions arising from water molecules located in the inner and outer shell of $\text{OH}^-(\text{H}_2\text{O})_{26}$. Some of these theoretical results provide valuable guidance for the interpretation of IRMPD spectra of small hydroxide-water clusters, but there are also several intriguing implications of these results, in particular, for the solvation of the OH^- ion at the surface of water nanodroplets and aqueous interfaces.

Received 5th June 2021,
Accepted 17th August 2021

DOI: 10.1039/d1cp02524d

rsc.li/pccp

I. Introduction

The hydroxide ion (OH^-) is next to the proton arguably the most important ion in nature. It is generated by the autoionization of water ($2\text{H}_2\text{O} = \text{OH}^- + \text{H}_3\text{O}^+$), and is involved in a wide range of inorganic hydrolysis and complexation equilibria, for example, as an active participant in RNA catalysis,^{1,2} and as a complexing ligand in environmentally important metal hydroxide nanoclusters.^{3,4} One of the more notable properties of the OH^- ion, is its propensity to form strong polarized hydrogen-bonds with water,⁵ leading to the formation of tightly bound solvation shells that serve as nucleation sites for water clusters and nanodroplets.⁶ There is also some debate on the nature of the hydroxide ion activity at the solution–gas interface, and the solvation environment preferred by the OH^- ion in the interfacial and bulk regions of liquid water.^{7–9} A variety of spectroscopic studies have suggested that the OH^- ion exhibits bulk preference,¹⁰ whereas H_3O^+ ions strive to become surface-solvated driven by enthalpy effects¹¹ with droplet/

cluster surface pH values of $\sim 3–5$.⁷ Results from IR studies of $\text{OH}^-(\text{H}_2\text{O})_n$ clusters,⁶ on the other hand, suggest that the OH^- ion occupies cluster surface sites in a manner similar to that observed for the solvated proton-water cluster system.¹² Therefore, in order to fully understand the solvation behavior of the hydroxide ion, and, in particular, its propensity for the surface, subsurface and bulk region of the air–water interface, it is essential to have a detailed description of the structures and IR spectral signatures of $\text{OH}^-(\text{H}_2\text{O})_n$ clusters.

Because of its central role in solution chemistry, interactions between OH^- and water molecules have been probed experimentally using ion mass spectrometry,^{5,13} IR spectroscopy,^{6,14,15} and theoretical calculations.^{16–24} On the experimental side, Yang *et al.* identified large $\text{OH}^-(\text{H}_2\text{O})_{1–60}$ clusters using ion mass spectrometry and revealed “magic-number” discontinuities at $n = 11, 14, 17$ and 20.²⁵ Other structure-sensitive spectroscopic studies reported infrared multi-photon dissociation (IRMPD) spectra for $\text{OH}^-(\text{H}_2\text{O})_{1–5}$ consistent with open solvation morphologies, where the OH^- ion is positioned at the water cluster surface.⁶ Results from Møller-Plesset perturbation theory (MP2) and coupled cluster CCSD(T) frequency calculations²¹ for $\text{OH}^-(\text{H}_2\text{O})_n$ are consistent with IRMPD studies of solvated hydroxide clusters, showing that surface solvation is favored for clusters with $n = 1–5$. In contrast, *ab initio* molecular dynamics simulations of larger $\text{OH}^-(\text{H}_2\text{O})_{47}$ clusters and $\text{OH}^-(\text{H}_2\text{O})_{71}$ slabs support the view that the OH^- ion accumulates

Department of Earth Sciences, University of Hong Kong, Pokfulam Road, Hong Kong, SAR. E-mail: kono@hku.hk; Fax: +852-2517-6912; Tel: +852-2241-5474

† Electronic supplementary information (ESI) available: Supporting Information I: MP2/aVDZ xyz coordinates of $\text{OH}^-(\text{H}_2\text{O})_n$ with $n = 8–26$. Supporting Information II: Fig. S1–S12. Relative energies, with (ΔE_e) and without ZPE-correction (ΔE_e), of $\text{OH}^-(\text{H}_2\text{O})_n$ isomers with $n = 8–26$ at the MP2/aVnZ, CCSD(T)/aVnZ and CCSD(T)/aVnZ:MP2/aVnZ levels of theory. See DOI: 10.1039/d1cp02524d

in the interior region of a water cluster, and is tetra-coordinated to water molecules.⁷ Thus, there appears to be a size-dependent structural transition in $\text{OH}^-(\text{H}_2\text{O})_n$, from surface to interior solvation that proceeds at approximately $n = 20\text{--}25$, and is quite comparable to the one observed in water clusters $(\text{H}_2\text{O})_n$ at $n = 16\text{--}17$.²⁶

The aim of this study is to examine the structures, energies and spectroscopic properties of $\text{OH}^-(\text{H}_2\text{O})_n$ clusters with $n = 8\text{--}26$ using artificial bee colony (ABC) algorithms²⁷ in conjunction with CCSD(T)/aVnZ//MP2/aVnZ ($n = \text{D}, \text{T}, \text{Q}$) methods and CPMD simulations.²⁸ Accordingly, this study expands on recent theoretical findings concerning the solvation of $\text{OH}^-(\text{H}_2\text{O})_n$ that employed correlated methods: for instance, MP2/CBS ($n = 4\text{--}16$), CCSD(T)/av(D,T)Z ($n = 1\text{--}4, 8$),¹⁷⁻¹⁹ MP2/aVDZ, CCSD(T)/VDZ ($n = 1\text{--}6$),¹⁸ MP2/CBS, CCSD(T)/aVTZ ($n = 4\text{--}6$),²⁹ CCSD(T)/aVTZ ($n = 1\text{--}4$)²¹ and CCSD(T)/aV(D,T)Z ($n = 1\text{--}5$).²³ Theoretical studies, in particular, high-level CCSD(T)/aVnZ ($n = \text{D}, \text{T}$) type calculations for clusters such as $(\text{H}_2\text{O})_{16,17}$, are time- and cpu-demanding and require in excess of 100 000 cores;²⁶ this challenge is further exacerbated by the large number of isoenergetic conformers that exist for $(\text{H}_2\text{O})_n$ and $\text{OH}^-(\text{H}_2\text{O})_n$ with $n > 8$. The approach adopted in the study aims to identify global minimum structures for $\text{OH}^-(\text{H}_2\text{O})_n$ with $n = 8\text{--}26$ using an ABC optimizer,²⁷ MP2 and CCSD(T) structure optimizations and frequency calculation. A previous study demonstrated that single point CCSD(T)/aVnZ ($n = \text{D}, \text{T}$) energies can be obtained for $(\text{H}_2\text{O})_{16,17}$ clusters using MP2/aVnZ ($n = \text{D}, \text{T}$) optimized geometries and harmonic zero-point energy (ZPE) corrections.²⁶ We have implemented a similar approach here to examine the effect of CCSD(T) correlation contribution on the stability of $\text{OH}^-(\text{H}_2\text{O})_n$ clusters up to $n = 26$, and evaluated CCSD(T)/aVnZ ($n = \text{D}, \text{T}$) energies for these clusters against those obtained from MP2 theory and two-layer ONIOM³⁰ CCSD(T)/aVnZ:MP2/aVnZ calculations. These results represent a considerable improvement in scope and accuracy over previous MP2 and CCSD(T) studies of solvated hydroxide clusters,¹⁷ and we will also see that the correct conformational sampling is a critical requirement for interpreting experimental data, in particular, from structure-sensitive IRMPD spectroscopy of $\text{OH}^-(\text{H}_2\text{O})_n$ clusters.⁶

Lin and coworkers³¹ reported MP2 and CCSD structures and energies for a wide range of cubic conformers for $\text{OH}^-(\text{H}_2\text{O})_7$ using MP2/6-311+G(d,p) optimizations, and conducted CCSD/6-311+G(d,p) SPC calculations on MP2 structures. Results from CCSD//MP2 calculations demonstrated that a cubic $\text{OH}^-(\text{H}_2\text{O})_7$ isomer dominated the population at $T < 200$ K, with strongly red-shifted OH stretching modes at 2310 cm^{-1} to 3250 cm^{-1} , due to ionic hydrogen bonds between water and the OH^- ion. These findings are broadly consistent with theoretical calculations for the hydroxyl radical clusters $\text{OH}^\bullet(\text{H}_2\text{O})_7$ and the water clusters $(\text{H}_2\text{O})_8$, and show that both clusters maintain a roughly cubic arrangement, where all water O atoms are 3-fold coordinated, with the hydroxyl radical folded along the edge of the cube.³² The situation is less clear for larger hydroxide-water clusters, even despite some recent remarkable experimental advances, in particular, from structure-sensitive IR spectroscopic studies of $\text{OH}^-(\text{H}_2\text{O})_n$ $n = 2\text{--}5$ ⁶ and $n = 8, 47$.¹⁵ For

example, results from MP2/aVDZ calculations of $\text{OH}^-(\text{H}_2\text{O})_n$ $n = 8, 12, 16$ found that the most stable $\text{OH}^-(\text{H}_2\text{O})_n$ geometries are structures in which hydroxide ions occupy apical positions of fused cubic water clusters.¹⁷ Results from recent B3LYP+D2/TZVP calculations for $\text{OH}^-(\text{H}_2\text{O})_n$ ($n = 6\text{--}11$) on the other hand, predict that the hydroxide ion is solvated at the edge of fused cubic water clusters, albeit with up to three free OH bonds rather than full H-bond connectivity.¹⁵ Thus, there is a critical need for accurate MP2 and CCSD(T) calculations of larger $\text{OH}^-(\text{H}_2\text{O})_n$ clusters in order to better understand the structural motifs involved in hydroxide hydration that will also lead to an improved consistency with existing IRMPD spectroscopic data.

The results from theoretical calculations presented in this study will provide answers to the following unresolved problems: (i) what structural features dominate the hydration environment in $\text{OH}^-(\text{H}_2\text{O})_n$ clusters, (ii) does the hydroxide ion reside in the interior or at the surface of the water cluster, and how does the solvation motif of OH^- vary as a function of cluster size, (iii) how does the choice of theory level, basis set size and zero-point energies influence the relative ordering in $\text{OH}^-(\text{H}_2\text{O})_n$ clusters, (iv) do $\text{OH}^-(\text{H}_2\text{O})_n$ clusters with particularly stable solvation structures exhibit characteristic IR spectral bands, and are these clusters therefore expected to be spectroscopically observable, and finally, (v) are there any other novel structures and spectroscopic features in $\text{OH}^-(\text{H}_2\text{O})_n$ clusters that are currently unknown?

II. Computational methods

All hydroxide-water cluster structures have been constructed using the following steps: (i) a library of ~ 200 $\text{OH}^-(\text{H}_2\text{O})_n$ structures was initially generated for $n = 8\text{--}26$ by means of an ABC algorithm²⁷ employing the TIP4P water³³ and hydroxide ion⁷ force field parameters, (ii) the resulting $\text{OH}^-(\text{H}_2\text{O})_n$ structures are then used as input for an initial M06-2X/aVDZ structure optimization and frequency calculation, (iii) followed by Møller-Plesset perturbation theory MP2/aVDZ and MP2/aVTZ re-optimizations and scaled frequency calculations (MP2/aVDZ: 0.959, MP2/aVTZ: 0.953), (iv) coupled cluster theory CCSD(T)/aVDZ single point calculations (SPC) for $n = 8\text{--}12$, and two-layer ONIOM³⁰ CCSD(T)/aVnZ:MP2/aVnZ ($n = \text{D}, \text{T}$) calculation for $n = 8\text{--}17, 23, 26$. All MP2, CCSD(T) and density functional theory calculations for $\text{OH}^-(\text{H}_2\text{O})_n$ have been undertaken using the Gaussian16 A.03 software package.³⁴ Geometry optimization and scaled harmonic frequency calculations were carried out using MP2, CCSD(T), M06-2X³⁵ and dispersion-corrected B3LYP-D3³⁶ in combination with correlation consistent double- ζ (aug-cc-pVDZ) and triple- ζ (aug-cc-pVTZ) basis sets³⁷ (abbrev. as aVDZ and aVTZ). The Boltzmann-averaged IR spectra for $\text{OH}^-(\text{H}_2\text{O})_{26}$ have been derived from their relative populations (calculated from their free energies at 300 K) using B3LYP-D3/aVDZ equilibrium structures and scaled (0.982) frequency calculations, and the spectral analysis was carried out using the Multiwfn³⁸ software package.

We also employed the two-layer ONIOM³⁰ method at the CCSD(T)/aVnZ:MP2/aVnZ level of theory to investigate the geometries and solvation energies of larger hydroxide–water clusters, in particular, for cubic and fused cubic OH[−](H₂O)₂₆ structures. In our ONIOM calculations, OH[−](H₂O)_n clusters are subdivided into two regions, and these are referred to as high- and low-level layers. For example, in OH[−](H₂O)₂₆, the high-level layer includes the primary solvation shell OH[−](H₂O)₆, and this region of the cluster is calculated at the CCSD(T)/aVDZ level, whereas a lower level of theory, *i.e.* MP2/aVDZ, is applied to the surrounding 20 second shell water molecules. In this approach, we treat the inner solvation shell in cubic OH[−](H₂O)₂₆ as the most important region, because of strong charge transfer interactions between the central OH[−] ion and first shell water molecules.

Ab initio molecular dynamics simulations have been performed using the Car–Parrinello method (CPMD) together with the Becke–Lee–Yang–Parr (BLYP)^{39,40} functional using a cut-off gradient correction of 5×10^{-6} . Vanderbilt ultrasoft pseudo-potentials were used for the O and H atoms and a plane wave point expansion with plane wave energy cutoffs of 25 Ry. The OH[−](H₂O)₂₆ cluster was set up at the center of a cubic simulation cell of size $21 \times 21 \times 21 \text{ \AA}^3$ with periodic boundary conditions, with the initial OH[−](H₂O)₂₆ isomer configuration taken from a combined artificial bee colony algorithm²⁷ and MP2/aVnZ ($n = D, T$) re-optimization scheme. Each CPMD system was initially equilibrated for 2–3 ps, followed by a 15 ps production simulation at a 0.096 fs step size. The temperature of the CPMD systems was kept constant by the Nosé–Hoover thermostat thereby ensuring proper canonical sampling at all temperatures, *i.e.* 50–300 K at 25 K step size. Power spectra at 50, 200, 250 and 300 K for inner and outer shell water molecules (*i.e.* bending, symmetric and antisymmetric stretching modes) for OH[−](H₂O)₂₆ were calculated from the Fourier transform of the velocity autocorrelation function (VACF) using the Travis trajectory analyzer.⁴¹

III. Results and discussion

A. CCSD(T) relative energies: fused cubic OH[−](H₂O)_{8–17}

We begin our discussion with the MP2/aVnZ ($n = D, T$) optimum structures and CCSD(T)/aVnZ ($n = D$) energies for the low-energy conformers of OH[−](H₂O)_n ($n = 8–26$), with a main focus on the propensity for surface *vs.* interior solvation of the OH[−] ion. Fig. 1 shows the global minima structures for $n = 8–26$, and the MP2/aVnZ and CCSD(T)/aVnZ energies for the most stable OH[−](H₂O)_n isomers in each cluster size are presented in the Fig. S1–S12 (ESI†). As seen from Fig. 1, the MP2/aVTZ optimized structure of OH[−](H₂O)₁₁, (labeled 11w-I) possesses a fused cubic framework, and corresponds, to the best of our knowledge, to a new global minimum. The optimal geometries of the five most stable isomers of OH[−](H₂O)₁₁, and their relative energies ΔE_e and ΔE_o are shown in the Fig. S4 (ESI†); we will see further below, these structures play a critical role as template and precursor for the growth of larger cubic hydroxide–water clusters. In the case of OH[−](H₂O)₁₂, the most

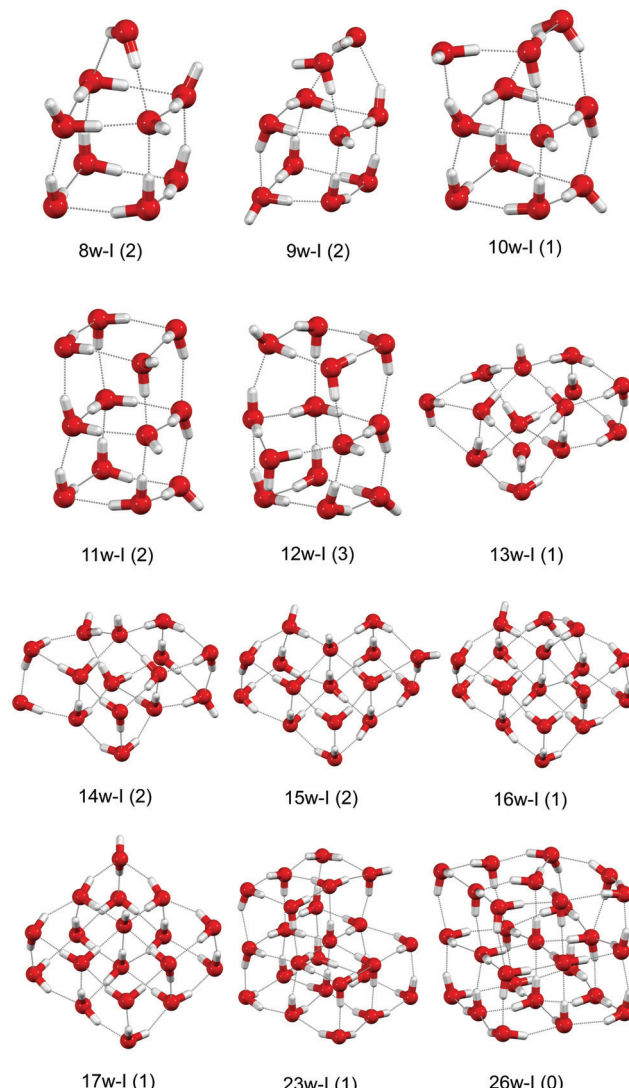


Fig. 1 MP2/aVTZ equilibrium structures of the lowest energy isomers for OH[−](H₂O)_{8–26}; number of dangling h-bonds given in parentheses.

stable isomer, (labeled 12w-I) in Fig. 1, consists of a five-membered OH[−](H₂O)₄ ring sandwiched between two antidiromic (H₂O)₄ ring systems (see Fig. S5 for OH[−](H₂O)₁₂ isomers, ESI†). Dixon and coworkers previously reported low-energy isomers of OH[−](H₂O)₁₂ with hydroxide ions positioned on the surface of homodromic networks of stacked (H₂O)₄ rings (12w-IV, Fig. S5, ESI†).¹⁷ A comparison of CCSD(T)/aVnZ//MP2/aVnZ energies for isomers of OH[−](H₂O)₁₂ suggest that isomer 12w-I is the lowest energy structure, with the previously reported isomer 12w-IV lying around 0.9 kcal mol^{−1} (MP2/aVTZ) and 0.6 kcal mol^{−1} (CCSD(T)/aVDZ) higher in energy. This difference reduces to around 0.3 kcal mol^{−1} with the inclusion of MP2/aVDZ ZPE-corrections corrections, however, with the caveat that MP2/aVDZ ZPE-corrections induce a reordering of OH[−](H₂O)₁₂ relative energies to 12w-II (most stable), 12w-I (0.04 kcal mol^{−1}), 12w-IV (0.24 kcal mol^{−1}), 12w-III (0.27 kcal mol^{−1}) and 12w-V (0.71 kcal mol^{−1}).

The MP2/aVnZ structures of larger $\text{OH}^-(\text{H}_2\text{O})_{13-17}$ clusters are also presented in Fig. 1 (MP2/aVTZ and CCSD(T)/aVnZ//MP2/aVnZ relative energies ΔE_e and MP2/aVnZ ZPE-corrected energies ΔE_o of the lowest energy isomers are shown in Fig. S6–S10 in the ESI†); it is noteworthy, that the most stable structures reported here, are structurally distinct, and all lower in energy than previously reported $\text{OH}^-(\text{H}_2\text{O})_n$ minima with $n = 13-17$. For instance, previously reported global minima for $\text{OH}^-(\text{H}_2\text{O})_{16}$ were found to be cube-like structure with the OH^- ion positioned at the tip of $(\text{H}_2\text{O})_{16}$ cages consisting of stacked cyclic tetramers.^{17,42} These $\text{OH}^-(\text{H}_2\text{O})_{16}$ structures were examined using DFT, MP2 and *ab initio* molecular dynamics calculations, and also included cuboid structures, double-ring and stacked 6-membered ring configurations. Our calculated MP2/aVnZ, CCSD(T)/aVnZ structures with MP2/aVnZ ZPE-corrections for $\text{OH}^-(\text{H}_2\text{O})_{16}$ are around $\sim 8-9$ kcal mol⁻¹ lower in energy than the cube-like $\text{OH}^-(\text{H}_2\text{O})_{16}$ clusters reported previously,¹⁷ and, thus, the later are not likely to be important among $n = 16$ structures. Instead, in the case of $\text{OH}^-(\text{H}_2\text{O})_{16}$, we identified 5 new clusters at the MP2/aVnZ and CCSD(T)/aVnZ:MP2/aVnZ level with the hydroxide O atom bound to a penta-coordinated site located on the surface of a fused cubic cluster (labeled 16w-I in Fig. 1). Four additional isomers labeled 16w-II, -III, -IV and -V fall within 0.5 kcal mol⁻¹ of the minimum energy structure 16w-I (see Fig. S9, ESI†), indicating that small structural changes in the hydrogen-bonding network of $\text{OH}^-(\text{H}_2\text{O})_{16}$ have a noticeable effect on the energetic ordering. MP2/aVnZ and CCSD(T)/aVnZ:MP2/aVnZ ($n = \text{D,T}$) calculations for $\text{OH}^-(\text{H}_2\text{O})_{17}$ suggest that there are at least five distinct and nearly isoenergetic structures (see Fig. S10, ESI†), with altered hydrogen-bonding patterns that fall within a narrow 0.1–0.5 kcal mol⁻¹ range of the global minimum cluster 17w-I. The $n = 17$ isomer 17w-I is also the MP2/aVnZ and CCSD(T)/aVnZ:MP2/aVnZ global minimum structure among all $\text{OH}^-(\text{H}_2\text{O})_{17}$ clusters when ZPE-corrections are included, and remains lowest in energy upon basis set expansion from aVDZ to aVTZ; this aspect is highlighted in Fig. S10 (ESI†) for $\text{OH}^-(\text{H}_2\text{O})_{17}$, which shows that as the basis set is extended, MP2/aVnZ and two-layer CCSD(T)/aVnZ:MP2/aVnZ relative energies ΔE_e and ΔE_o are in all cases relatively similar.

B. MP2 and CCSD(T) relative energies: cubic $\text{OH}^-(\text{H}_2\text{O})_{26}$

Fig. 2a and b shows the global minima structures and energies ΔE_e and ΔE_o for $\text{OH}^-(\text{H}_2\text{O})_{26}$ that have been calculated at the MP2/aVnZ and CCSD(T)/aVnZ:MP2/aVnZ level of theory, and these are predicted to be compact $3 \times 3 \times 3$ clusters with a hexa-coordinated OH^- ion positioned at the center of a cubic $(\text{H}_2\text{O})_{25}$ network. We identified three low-lying, almost isoenergetic cubic $\text{OH}^-(\text{H}_2\text{O})_{26}$ clusters (labeled 26w-I, -II–III in Fig. 2a) within a narrow energy window of ~ 0.2 kcal mol⁻¹, and with different hydrogen-bonding patterns; Fig. 2b also shows stable $\text{OH}^-(\text{H}_2\text{O})_{26}$ conformers with the OH^- ion residing at the surface of cubic (26w-VII), chair- (26w-VI) and plate-like (26w-VIII) structures. It is worth noting that, basis set expansion from MP2/aVDZ to MP2/aVTZ, induces a change in the ordering of the relative energy ΔE_e for $\text{OH}^-(\text{H}_2\text{O})_{26}$, with isomer

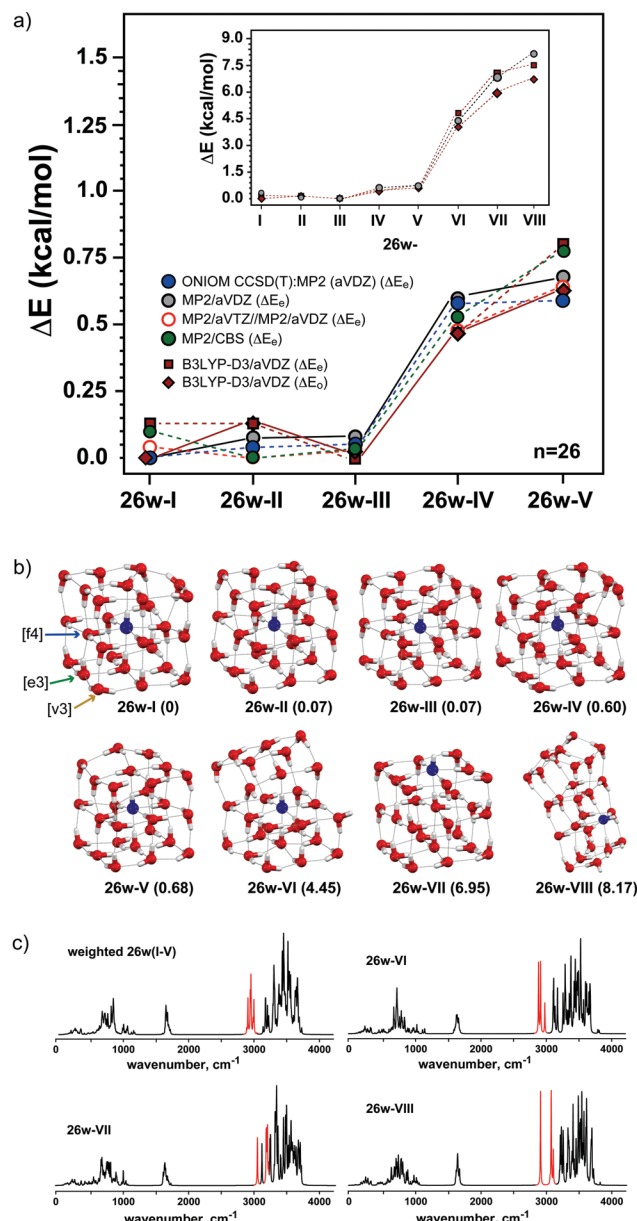


Fig. 2 Stable configurations of $\text{OH}^-(\text{H}_2\text{O})_{26}$. (a) CCSD(T)/aVnZ:MP2/aVnZ, MP2/aVnZ electronic (ΔE_e) and B3LYP-D3/aVDZ ZPE-corrected (ΔE_o) relative energies in kcal mol⁻¹ of the five most stable cubic $\text{OH}^-(\text{H}_2\text{O})_{26}$ conformers. (b) MP2/aVDZ structures and relative energies (ΔE_e) of eight cubic and fused cubic $\text{OH}^-(\text{H}_2\text{O})_{26}$ conformers, five with the OH^- ion positioned in the interior of the cube and three (26w-VI, -VII, -VIII) favoring hydroxide surface solvation. (c) Boltzmann-averaged IR spectra for interior 26w(I–V), and IR spectra for surface-solvated clusters 26w-VI, -VII, -VIII derived from relative free energies at the B3LYP-D3/aVDZ level at 300 K.

26w-II being more stable (by ~ 0.1 kcal mol⁻¹) than isomer 26w-I, and thus, although being well within the chemical accuracy limit of 1 kcal mol⁻¹, the ordering of ΔE_e is still quite sensitive to the size of the basis set. We also computed MP2 energies ΔE_e using a two-point (aVDZ and aVTZ) CBS extrapolation scheme,⁴³ and, as seen from Fig. 2, the ΔE_e order remains unchanged following extrapolation to the CBS limit: 0.0 kcal mol⁻¹ (26w-II), 0.04 kcal mol⁻¹

(26w-III), 0.10 kcal mol⁻¹ (26w-I), 0.53 kcal mol⁻¹ (26w-IV) and 0.77 kcal mol⁻¹ (26w-IV). The inclusion of ZPE corrections, albeit at the B3LYP-D3 level of theory, was found to introduce a small but noticeable effect on the relative energies ΔE_o and ordering among the 5 cubic OH⁻(H₂O)₂₆ isomers 26w(I-VI). B3LYP-D3 results for ΔE_o predict the relative order: 26w-I (most stable), 26w-III (0.03 kcal mol⁻¹), 26w-II (0.12 kcal mol⁻¹), 26w-IV (0.47 kcal mol⁻¹) and 26w-V (0.62 kcal mol⁻¹), and this ordering is shown in Fig. 2a where the red solid lines (and diamond symbols) trace the relative stabilities of the cubic OH⁻(H₂O)₂₆ clusters when ZPE-corrections are taken into account. These results indicate that the structures of OH⁻(H₂O)₂₆ are stabilized through strong ionic hydrogen-bonds at the cluster core, and through a network of hydrogen bonds involving water molecules at vertices, edges and face-sites of a cubic OH⁻(H₂O)₂₅ network. Based on MP2/aVDZ calculations for the OH⁻(H₂O)₂₆ isomer 26w-I, we find that the tetra-coordinated H₂O face-sites (labeled f4, blue arrow, Fig. 2b) are around 10 kcal mol⁻¹ more stable than tri-coordinated H₂O edge-sites (labeled e3, green arrow), and 14 kcal mol⁻¹ more stable than those in which H₂O occupies vertices (labeled v3, brown arrow) of the OH⁻(H₂O)₂₆ cluster. These differences in stability are also reflected in the MP2/aVDZ OH⁻(H₂O)₂₅ (i) face-, (ii) edge- and (iii) vertex hydration energies, which are 33.7 kcal mol⁻¹, 23.3 kcal mol⁻¹ and 19.8 kcal mol⁻¹, per water molecule, respectively.

We also evaluated equilibrium structures and vibrational frequencies of cubic OH⁻(H₂O)₂₆ clusters using two-layer CCSD(T)/aVDZ:MP2/aVDZ, MP2/aVDZ and B3LYP-D3/aVDZ level of theory. As seen from Fig. 2a and b, these methods yield consistent electronic energies and ZPE corrections for similar global and local minimum structures. For OH⁻(H₂O)₂₆, all three methods accurately reproduce the energetic rankings (without and with ZPE-correction, see Fig. 2a), and provide similar vibrational frequencies for the same cluster type. For example, when B3LYP-D3/aVDZ energies are considered (with and without ZPE corrections), the energetic ordering remains unchanged relative to results from higher accuracy MP2 calculations (see insert Fig. 2a). Both MP2 and B3LYP-D3 predict three nearly isoenergetic cubic OH⁻(H₂O)₂₆ clusters (labeled 26w-I, -II, -III in Fig. 2), closely followed by two higher energy isomers (labeled 26w-IV, -V), that are ~0.6 kcal mol⁻¹ higher in energy than the OH⁻(H₂O)₂₆ global minimum structure 26w-I. MP2 and B3LYP-D3 calculations show that the five cubic OH⁻(H₂O)₂₆ clusters 26w(I-V) have a relatively shallow potential energy surface around the global minimum, and thus, are well described by the Boltzmann-weighted average of the IR spectra of each isomer (see Fig. 2c). All five cubic OH⁻(H₂O)₂₆ clusters display significantly red-shifted OH-stretching bands below ~2900 cm⁻¹, and this feature is a direct consequence of strong intermolecular hydrogen bonds between the central OH⁻ ion, and the surrounding water molecules in the primary hydration shell. These strongly red-shifted OH-stretching bands are also observed between 2880 cm⁻¹ and 3110 cm⁻¹ in the IR spectra of the chair-like OH⁻(H₂O)₂₆ isomer 26w-VI. These bands, however, are noticeably absent from the 2800–3100 cm⁻¹ region of IR spectra of the surface-hydrated isomer 26w-VII, indicating a significant difference in the IR

spectra of surface and interior structures of cubic OH⁻(H₂O)₂₆ clusters. Interestingly, results shown in Fig. 2a and b also indicate that among all OH⁻(H₂O)₂₆ clusters, structure 26w-I is the most thermodynamically stable, having the largest negative binding energy (~398.9 kcal mol⁻¹ with MP2/aVDZ, and ~393.6 and ~409.1 kcal mol⁻¹ with M06-2X/aVDZ and B3LYP-D3/aVDZ, respectively). Building on these results, we have performed a series of *ab initio* molecular dynamics simulations over the temperature range from 50 K to 300 K to examine the structural, dynamic and spectroscopic features of the OH⁻(H₂O)₂₆ global minimum isomer 26w-I.

C. CPMD of cubic OH⁻(H₂O)₂₆: surface *versus* interior solvation

Panel (a) of Fig. 3 shows representative OH⁻(H₂O)₂₆ cluster structures obtained from CPMD simulations over the temperature range 50 K to 300 K, each snap shot covering the final 4 ps of the full 16 ps simulation trajectory. Also shown are the hydroxide O (O_{OH}) and water O atom (O_w) O_{OH}–O_w radial distribution functions (RDF) $g_{O-O}(r)$, running coordination numbers $n_{O-O}(r)$ of H₂O molecules surrounding the OH⁻ ion, and structural and thermodynamic properties relevant to the stability of OH⁻(H₂O)₂₆ (see Fig. 3b and c). At 50 K, the primary and secondary solvation shells are at 2.75 ± 0.06 Å and 4.17 ± 0.09 Å; these features are sharply defined and integrate up to exactly 6 and 14 oxygen atoms, respectively, with the primary OH⁻(H₂O)₆ shell maintaining octahedral coordination. We find that with increasing temperature (from 50 K to 150 K), the O_{OH}–O_w distances of first shell waters are constant at 2.75 Å, whereas $r_{O_{OH}-O_w}$ values of secondary shell waters increase to 4.25 Å. Starting at 150 K, the second (4.25 Å) and third (5.2 Å) hydration shell peaks around OH⁻ begin to disappear (as a consequence of the weakening of the H-bonding network upon heating), and eventually, at around 180–200 K, merge into a broad single peak structure ranging from 4.25 to 5.30 Å. Fig. 3a shows that the octahedral OH⁻(H₂O)₆ core is rigid, and remains fully preserved throughout the timescale of the trajectory and up to ~200 K. Beginning at 200 K, however, the OH⁻(H₂O)₆ core structure is lost, and gradually transforms from octahedral, to tetrahedral OH⁻(H₂O)₄, and finally to a distorted trigonal-pyramidal OH⁻(H₂O)₃ coordination at 300 K. These simulations demonstrate that the OH⁻ ion is buried inside the cavity of the cubic (H₂O)₂₆ cluster at temperatures up to around 200 K, and, upon heating from 200 to 300 K, transfers to a surface-exposed position with reduced coordination numbers. i.e. $n_{O-O}(r) = 3\text{--}4$, and a maximum of 24 dangling (non-hydrogen-bonding) OH groups (see Fig. 3c, center).

Fig. 4a–c presents typical structures of the solvated OH⁻ ion together with first-shell water molecules (labeled in blue), with each panel displaying snapshots taken from the final 4 ps of the CPMD simulation at 50, 250 and 300 K. To explore this further, we examined the structure and temporal stability of the inner region of the OH⁻(H₂O)₂₆ cluster using two structural parameters: the $r_{O_{OH}-O_w}$ distance and the dihedral angle (DHA), which characterizes the rigidity and extent of planarity of the equatorial water ligands in the primary solvation shell. These

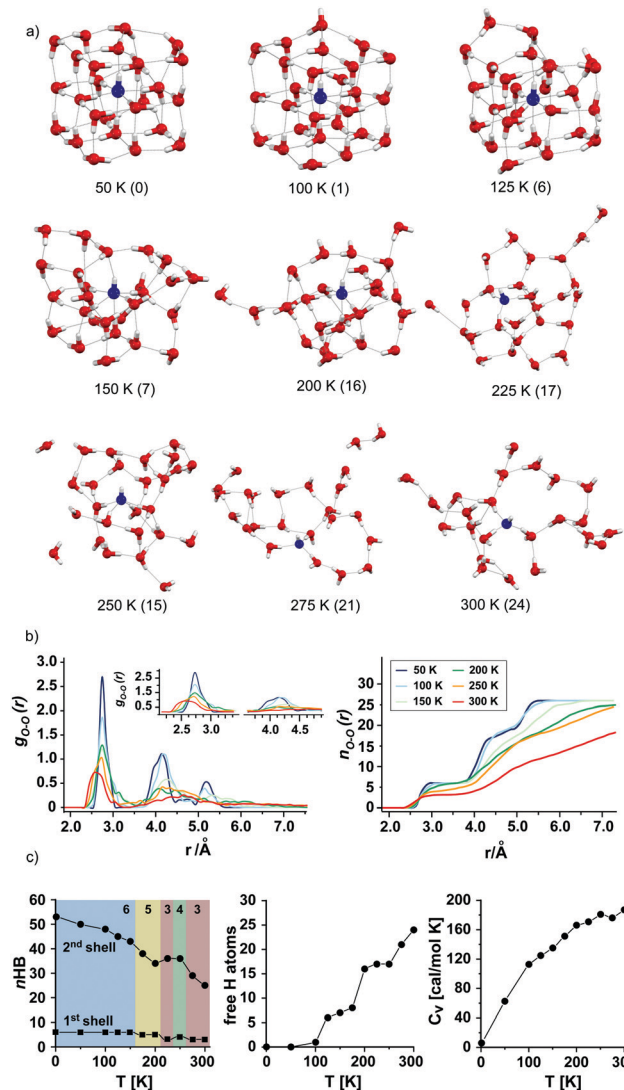


Fig. 3 Solvation structures and stability of the cubic $\text{OH}^-(\text{H}_2\text{O})_{26}$ cluster 26w-I at 50–300 K. (a) Representative structures of $\text{OH}^-(\text{H}_2\text{O})_{26}$ isomer 26w-I with the number of free H atoms given in parentheses, hydroxide O atom in blue. (b) Radial distribution function $g_{\text{O}-\text{O}}(r)$ and running coordination number $n_{\text{O}-\text{O}}(r)$ from 50 K to 300 K for $\text{OH}^-(\text{H}_2\text{O})_{26}$. (c) Temperature-dependent number of first and second hydration shell h-bonds; average number of free H atoms and molecular heat capacity.

structural features are obtained by calculating the time-averaged dihedral angle distribution functions (ADF) and $r_{\text{O}_{\text{OH}}-\text{O}_w}$ distances at different temperatures.

The dihedral angle ($\text{O}_0-\text{O}_1-\text{O}_2-\text{OH}$) at 50 K in $\text{OH}^-(\text{H}_2\text{O})_6$ is close to 60° , and fluctuates in the range of 50° to 65° , while distorted configurations beyond 70° are very rarely observed (see Fig. 4a); the time-averaged $r_{\text{O}_{\text{OH}}-\text{O}_w}$ distance for first shell water at 50 K is about $2.75 \pm 0.06 \text{ \AA}$, and this distance gradually increases from $2.82 \pm 0.09 \text{ \AA}$ (100 K), $2.90 \pm 0.17 \text{ \AA}$ (150 K) to $2.89 \pm 0.15 \text{ \AA}$ (200 K). Taken together, RDF and ADF calculations clearly underscore the affinity of the OH^- ion for the cluster interior and the high structural rigidity of the $\text{OH}^-(\text{H}_2\text{O})_{26}$ geometry up to around 200 K. These results differ significantly from those at 250 K, and are of particular interest,

in that they offer a unique view of the hydration environment upon transfer of the OH^- ion from the interior to the surface of the water cluster. The general picture that emerges suggests a dynamical shift from a compact 6-fold hydration shell at lower-temperatures (50–200 K), towards a surface-solvated ion with 4 first-shell water molecules at 250 K as shown in Fig. 4b. These water molecules attach *via* four short ionic hydrogen-bonds to the central OH^- ion, with a $r_{\text{O}_{\text{OH}}-\text{O}_w}$ distance at 250 K of $2.75 \pm 0.14 \text{ \AA}$. Interestingly, these results appear to suggest that the solvation of OH^- in a small water cluster at 250 K gives rise to a very different local hydration scenario compared to results from gas-phase results of $\text{OH}^-(\text{H}_2\text{O})_n$ clusters for $n = 1-5$,⁶ i.e. a primary hydration shell consisting of four water molecules that H-bond directly onto the central ion *versus* a structure involving three first-shell waters and a fourth water that binds *via* a double-donor configuration to the primary solvation shell rather than directly to the OH^- ion.

Fig. 4c also presents the time-averaged ADFs and $r_{\text{O}_{\text{OH}}-\text{O}_w}$ distances for the inner $\text{OH}^-(\text{H}_2\text{O})_3$ core for the final 4 ps of the simulation at 300 K. From the ADF plot we can see that the distribution of the $\text{O}_0-\text{O}_1-\text{O}_3-\text{OH}$ dihedral angle at 300 K (Fig. 4c, right panel) falls broadly into two groups at 55° and 25° , reflecting the gradual transition from a tetra- to tri-coordinated structure with time, with the OH^- ion at the center of a distorted trigonal- $\text{OH}^-(\text{H}_2\text{O})_3$ cluster and $r_{\text{O}_{\text{OH}}-\text{O}_w} = 2.69 \pm 0.10 \text{ \AA}$; this solvation motif remains unchanged for the remaining 5 ps simulation time, in other words, the structure does not revert back to a 4-fold coordinated OH^- ion. As shown in Fig. 3b, RDF peaks stemming from second and third solvation shells at 300 K are rather poorly defined and appear as broad features ranging from 3.5–6.0 \AA . Therefore, at 300 K, the $\text{OH}^-(\text{H}_2\text{O})_3$ cluster organizes all three first shell water molecules in at relatively short distances of about 2.7 \AA . As a consequence, first shell RDF's appear as distinct peaks as shown in Fig. 3b, whereas broader RDF peaks, features typical of a disordered liquid (or even dense water vapor), characterize the distribution of water molecules at the surface of $\text{OH}^-(\text{H}_2\text{O})_3$ and in the long-range dynamical solvation shell.

D. Temperature-dependent power spectra of $\text{OH}^-(\text{H}_2\text{O})_{26}$

Finally, we discuss the vibrational power spectra for $\text{OH}^-(\text{H}_2\text{O})_{26}$ that have been computed using the Fourier transform of the velocity autocorrelation function (VACF) at 50, 200, 250 and 300 K, and for different regions of the solvation shell (see Fig. 4d and e). The peak at $\sim 1600 \text{ cm}^{-1}$ in Fig. 4d represents the water bending vibration (ν_2), and the two overlapping vibrational regions from 2770 to 3780 cm^{-1} , correspond to the symmetric (ν_1) and anti-symmetric (ν_3) OH stretching bands. For the bending mode, we find that an increase in temperature from 50 to 300 K causes the maximum of the water ν_2 bending band to become red-shifted (by $\sim 30 \text{ cm}^{-1}$), and split into three distinct bands, with a broad spectral feature at 1598 cm^{-1} , and two weaker shoulder peaks at 1390 cm^{-1} and 1685 cm^{-1} . Thus, the maximum of the ν_2 band shifts systematically with increasing temperature from 1628 cm^{-1} (50 K), 1626 cm^{-1} (100 K), 1613 cm^{-1} (150 K), 1603 cm^{-1} (200 K) to 1598 cm^{-1} (300 K) (see insert Fig. 4d), increases notably in intensity, and further splits into one major and two sub-peaks at

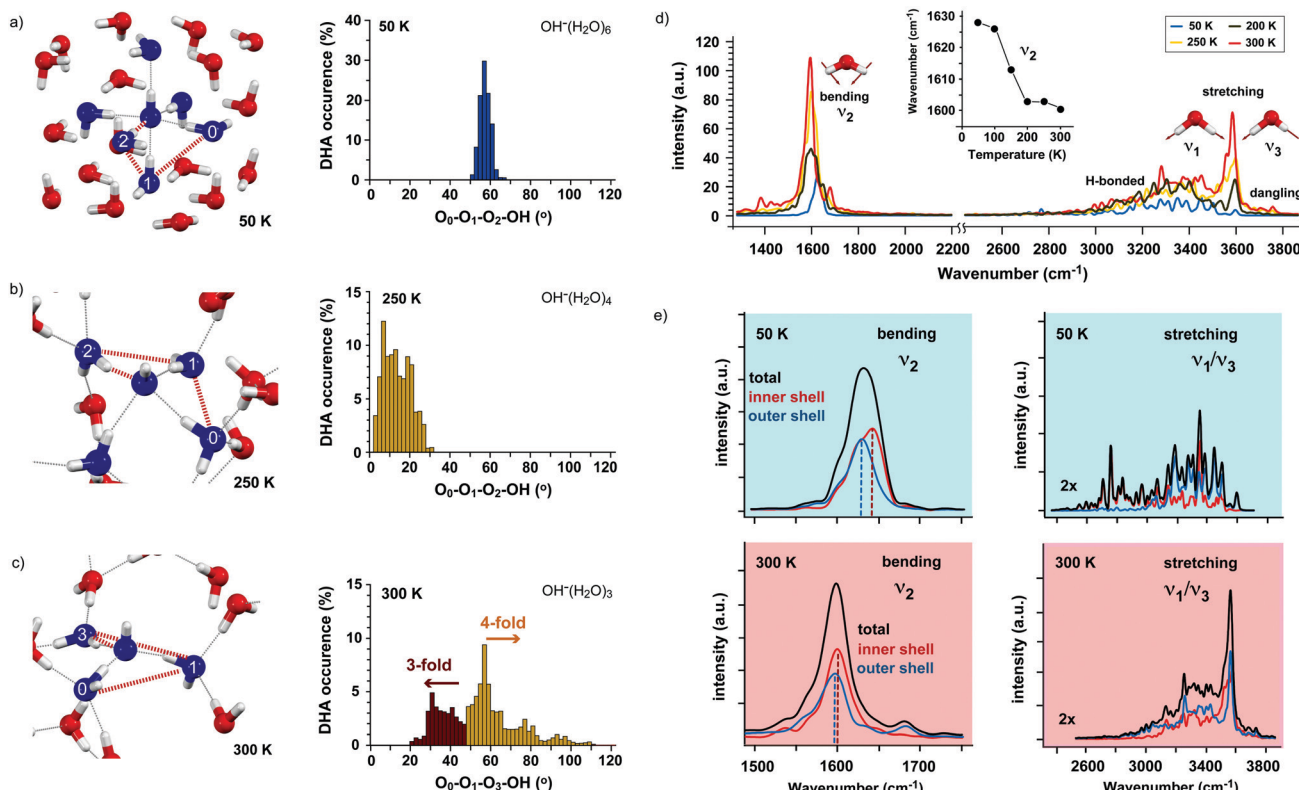


Fig. 4 Spatial organization, angular distribution function (ADF) and power spectra of inner and outer shell waters in OH⁻(H₂O)₂₆ isomer 26w-I (a–c). Inner solvation shell configuration and distribution of dihedral angles at 50, 250 and 300 K. (d) Temperature-dependent vibrational power spectra of water molecules for OH⁻(H₂O)₂₆ with H–O–H bending and OH-stretching bands at 1390–1685 cm⁻¹ and 2950–3750 cm⁻¹, respectively; inset shows the shift of the peak maxima of the ν₂ bending band with temperature. (e) Inner (red) and outer solvation shell (blue) vibrational power spectra at 50 and 300 K.

300 K owing to the disruption of the hydrogen bond network in OH⁻(H₂O)₂₆. Interestingly, the observed red-shift of the bending frequency with temperature amounts to around 0.1 cm⁻¹ K⁻¹, which is in overall good agreement with the experimental value of 0.05 cm⁻¹ K⁻¹ (albeit from a different temperature range, *i.e.* 295–373 K).⁴⁴ Furthermore, the bending mode frequencies of inner shell water molecules at 50 K in OH⁻(H₂O)₂₆ tend to be blue-shifted (by ~20 cm⁻¹), relative to bending modes of waters located at the cluster surface, indicating the presence of two different classes of water molecules (see Fig. 4e). This observation somewhat contradicts the expectation that the bending frequencies of inner shell water will be red-shifted due to the presence of strong ionic hydrogen-bond interactions, and the stiffening of the water network structure around the OH⁻ ion. The observed blue-shift of inner shell water, however, can be understood in light of recent IR spectroscopic results on the variation of the H–O–H bending mode in small anion water clusters, where even larger (~120 cm⁻¹) blue-shifted water bending modes are shown to exist in the IR spectra of solvated gas-phase ion clusters such as NO₃⁻(H₂O)_{1–6}⁴⁵ and HCO₃⁻(H₂O)_{1–10}.⁴⁶

Similar spectral features are also observed in the ν₁ and ν₃ stretching bands of water at 50 and 300 K. Fig. 4d shows that, as the temperature increases, the line shapes and positions of the OH-stretching modes differ considerably from those observed at lower temperatures. For example, the antisymmetric OH-stretching

mode frequencies are blue-shifted to higher frequencies (by ~150 cm⁻¹) with increasing temperature, and the absorption intensity of these bands increase, probably because of the rupture of hydrogen bonds in OH⁻(H₂O)₂₆ and the emergence of dangling OH bonds at the cluster surface. In order to uncover the origin of these spectral features, we also calculated the temperature-dependent changes in the symmetric ν₁ and asymmetric ν₃ OH stretching vibrational frequencies of water molecules in the inner solvation shell region, located at 3.0–3.5 Å distance from the OH⁻ ion, and for water molecules beyond 4 Å, *i.e.* within the outer shell (see Fig. 4e).

The ν₁ OH-stretching modes of inner shell water molecules at 50 K are strongly red-shifted, appear at lower frequencies near 2580 cm⁻¹, and extend up to approximately 3480 cm⁻¹ (Fig. 4e, red trace 50 K); these inner shell water molecules are locked into a rigid hydrogen-bond network that is further reinforced by strong electrostatic interactions between H₂O molecules and the OH⁻ ion. The ν₁ and ν₃ OH-stretching modes of outer shell waters at 50 K (Fig. 4e, blue trace), on the other hand, appear at considerably higher frequencies (3050–3575 cm⁻¹), relative to OH-stretching bands arising from inner shell water molecules. This blue-shift in the ν₁ and ν₃ stretching modes of outer shell waters is a direct consequence of the presence of a small, but steadily growing, number of dangling OH groups at the surface of the OH⁻(H₂O)₂₆ cluster. Fig. 4e also displays vibrational spectra for the inner- and outer-shell solvation

environment at higher temperature, *i.e.* 300 K. These data show that an increase in temperature from 50 to 300 K induces a broadening and blue shift of the OH-stretching mode frequencies for both inner and outer solvation shell waters. As is displayed in Fig. 4e, this joint broadening and blue shift of inner- and outer-shell OH stretching mode frequencies shows that the hydration network around the OH⁻ ion transforms from a cubic ice-like “solid” to a disordered configuration akin to a water vapor-like environment, and therefore, a clear-cut distinction between both solvation regions is gradually lost with increasing temperature. In summary, Fig. 4d and e shows that as the temperature increases from 50 to 300 K, the peak maxima of the ν_1 symmetric stretching mode frequency blue shifts significantly (from ~ 2780 to $\sim 3120\text{ cm}^{-1}$), and increases in intensity due to deformation and structural fluctuation of the cluster. For the positions of the peak maxima of the ν_3 stretching bands, we observed a slightly less pronounced blue-shift with increasing temperature (from around 3380 to 3490 cm^{-1}), resulting in a broad spectral feature ranging from 2950 to 3750 cm^{-1} ; these findings are also consistent with the ν_2 bending bands being red-shifted and split (as the temperature increases from 50 to 300 K), which are dominated by the strong absorption of H-O-H bending bands of free water molecules at $\sim 1575\text{ cm}^{-1}$ that have detached from the OH⁻(H₂O)₂₆ cluster.

To summarize, electronic structure calculations have been employed to examine the structure, stability and solvation dynamics of the hydroxide ion. Results from these studies allow us to assess the effects of temperature and simulation time on the solvation dynamics and hydrogen-bonding around the OH⁻ ion, and more importantly, the hydroxide ions’ propensity for the water cluster surface (or near-surface) region. We anticipate that these findings will not only be relevant in the context of hydroxide nanosolvation, but also critical in understanding molecular-scale ionization reactions in water nanodroplets and at the liquid water surface. For example, answers to these questions are relevant to the temperature- and size-dependence of water cluster pK_w values⁴⁷ and ultimately the pH of water vapor.⁴⁸

IV. Conclusions

In this work we have employed MP2, CCSD(T) and *ab initio* molecular dynamics simulations to probe the structure and dynamic stability of the OH⁻ ion in small clusters with up to 26 water molecules. Results from MP2 calculations point towards a new set of OH⁻(H₂O)_n clusters with cubic and fused cubic global minima structures for $n = 11\text{--}26$. These results support the view that the solvated hydroxide ion transitions from an “all-surface” motif at $n = 17\text{--}20$ to an internally solvated cluster configuration at $n = 26$. Our CCSD(T) level calculations confirm a structural transition from surface-to-interior solvation for $n = 26$, pointing to an increasing affinity of the OH⁻ ion for the water cluster interior as the cluster size evolves beyond $n \sim 20$.

Results from *ab initio* molecular dynamics simulations of OH⁻(H₂O)₂₆ demonstrate that the hydroxide ion remains in the

cluster interior and hexa-coordinated, irrespective of the temperature, up to around 175 K. At higher temperatures, the solvation environment incrementally transitions from a surface exposed penta- (170–200 K), tetra- (225 K) to a tri-coordinated ($> 225\text{ K}$) OH⁻(H₂O)₃ cluster. Based on our temperature-dependent vibrational power spectra, we estimate that the peak maximum of the HOH bending mode ν_2 (1628 cm^{-1}) in the IR spectra of the cubic OH⁻(H₂O)₂₆ cluster 26w-I at 50 K red-shifts by 30 cm^{-1} , and is further split into two sub-peaks at 1390 cm^{-1} and 1685 cm^{-1} upon heating to 300 K. The situation is completely the opposite in the case of the OH stretching bands: OH-stretching bands (from 2580 cm^{-1} to $\sim 2900\text{ cm}^{-1}$) present in the IR spectra of the OH⁻(H₂O)₂₆ cluster 26w-I at 50 K are almost completely lost in the 300 K power spectra, and gradually merge with increasing temperature into a broad band of approximately 270 cm^{-1} width with a peak maximum centered at 3590 cm^{-1} , and a weaker OH stretching band at 3285 cm^{-1} . We believe that these results point towards a strong correlation between hydrogen bond strength and OH stretching vibration, *i.e.* an increase in temperature from 50 to 300 K results in a weakening of the intermolecular O· · · H hydrogen-bond which in turn leads to a blue-shift of the OH stretching modes by up to 230 cm^{-1} . In the case of the HOH bending mode frequency ν_2 , we see that the same temperature dependence manifests itself in a red-shift in the bending modes, from 1627 cm^{-1} to 1598 cm^{-1} , owing to the weakening of the intermolecular hydrogen bonds in OH⁻(H₂O)₂₆.

Conflicts of interest

There are no conflicts to declare.

Acknowledgements

I would like to thank David Phillips and Wallace Hui for helpful discussions. This research was supported by the HK General Research Fund HKU (Grant No. P17330216 and P17307118). Computing time for this study was provided to K. H. L. by the HKU High Performance Computing (Grant No. HPC2015) Center.

References

- 1 M. J. Fedor and J. R. Williamson, *Nat. Rev. Mol. Cell Biol.*, 2005, **5**, 399–412.
- 2 H. Lönnberg, *Org. Biomol. Chem.*, 2011, **9**, 1687–1703.
- 3 W. H. Casey, B. L. Phillips and G. Furrer, *Rev. Min. Geochem.*, 2001, **44**, 167–190.
- 4 W. H. Casey, *Chem. Rev.*, 2006, **106**, 1–16.
- 5 M. Meot-Ner and C. V. Speller, *J. Phys. Chem.*, 1986, **90**, 6616–6624.
- 6 W. H. Robertson, E. G. Diken, E. A. Price, J. W. Shin and M. A. Johnson, *Science*, 2003, **299**, 1367–1372.
- 7 R. Vácha, V. Buch, A. Milet, D. P. Devlin and P. Jungwirth, *Phys. Chem. Chem. Phys.*, 2007, **9**, 4736–4747.

- 8 S. Das, M. Bonn and E. H. Backus, *Angew. Chem., Int. Ed.*, 2019, **58**, 15636–15639.
- 9 C. J. Mundy, I. F. W. Kuo, M. E. Tuckerman, H. S. Lee and D. J. Tobias, *Chem. Phys. Lett.*, 2009, **481**, 2–8.
- 10 B. Winter, M. Faubel, R. Vácha and P. Jungwirth, *Chem. Phys. Lett.*, 2009, **474**, 241–247.
- 11 S. Das, S. Imoto, S. Sun, Y. Nagata, E. H. Backus and M. Bonn, *J. Am. Chem. Soc.*, 2019, **142**, 945–952.
- 12 J. M. Headrick, E. G. Diken, R. S. Walters, N. I. Hammer, R. A. Christie, J. Cui, E. M. Myshakin, M. A. Duncan, M. A. Johnson and K. D. Jordan, *Science*, 2005, **308**, 1765–1769.
- 13 G. J. Paul and P. Kebarle, *J. Phys. Chem.*, 1990, **94**, 5184–5189.
- 14 O. Gorlova, J. W. DePalma, C. T. Wolke, A. Brathwaite, T. T. Odbadrakh, K. D. Jordan, A. B. McCoy and M. A. Johnson, *J. Chem. Phys.*, 2016, **145**, 134304.
- 15 J. Lengyel, M. Ončák, A. Herburger, C. van der Linde and M. K. Beyer, *Phys. Chem. Chem. Phys.*, 2017, **19**, 25346–25351.
- 16 S. S. Xantheas, *J. Am. Chem. Soc.*, 1995, **117**, 10373–10380.
- 17 C. G. Zhan and D. A. Dixon, *J. Phys. Chem. A*, 2002, **106**, 9737–9744.
- 18 H. M. Lee, P. Tarkeshwar and K. S. Kim, *J. Chem. Phys.*, 2004, **121**, 4657–4664.
- 19 F. C. Pickard IV, E. K. Pokon, M. D. Liptak and G. C. Shields, *J. Chem. Phys.*, 2005, **122**, 024302.
- 20 V. S. Bryantsev, M. S. Diallo, A. C. van Duin and W. A. Goddard III, *J. Chem. Theory Comput.*, 2009, **5**, 1016–1026.
- 21 R. Roszak, R. W. Góra and S. Roszak, *Int. J. Quantum Chem.*, 2012, **112**, 3046–3051.
- 22 Y. Crespo and A. Hassanali, *J. Chem. Phys.*, 2016, **144**, 074304.
- 23 C. K. Egan and F. Paesani, *J. Chem. Theory Comput.*, 2018, **14**, 1982–1997.
- 24 F. Calvo, *Mol. Simul.*, 2019, **45**, 269–278.
- 25 X. Yang and A. W. Castleman, *J. Phys. Chem.*, 1990, **94**, 8500–8502.
- 26 S. Yoo, E. Apra, X. C. Zeng and S. S. Xantheas, *J. Phys. Chem. Lett.*, 2010, **1**, 3122–3127.
- 27 J. Zhang and M. Dolg, *Phys. Chem. Chem. Phys.*, 2016, **18**, 3003–3010.
- 28 J. Hutteret *et al.* CPMD: An Ab Initio Electronic Structure and Molecular Dynamics Program, see <http://www.cpmd.org>.
- 29 X. Sun, S. Yoo, S. S. Xantheas and L. X. Dang, *Chem. Phys. Lett.*, 2009, **481**, 9–16.
- 30 S. Dapprich, I. Komáromi, K. S. Byun, K. Morokuma and M. J. Frisch, *J. Mol. Struct.: THEOCHEM*, 1999, **461**, 1–21.
- 31 R. J. Lin, Q. C. Nguyen, Y. S. Ong, K. Takahashi and J. L. Kuo, *Phys. Chem. Chem. Phys.*, 2015, **17**, 19162–19172.
- 32 S. D. Belair, J. S. Francisco and S. J. Singer, *Phys. Rev. A: At., Mol., Opt. Phys.*, 2005, **71**, 013204.
- 33 W. L. Jorgensen, J. Chandrasekhar, J. D. Madura, R. W. Impey and M. L. Klein, *J. Chem. Phys.*, 1983, **79**, 926–935.
- 34 M. J. Frischet *et al.* Gaussian 09, Revision A.03, Gaussian, Inc., Wallingford, CT, 2016.
- 35 Y. Zhao and D. G. Truhlar, *Theor. Chem. Acc.*, 2008, **120**, 215–241.
- 36 S. Grimme, J. Antony, S. Ehrlich and H. Krieg, *J. Chem. Phys.*, 2010, **132**, 154104.
- 37 T. H. Dunning Jr., *J. Chem. Phys.*, 1989, **90**, 1007–1023.
- 38 T. Lu and F. Chen, *J. Comput. Chem.*, 2012, **33**, 580–592.
- 39 A. D. Becke, *Phys. Rev. A: At., Mol., Opt. Phys.*, 1988, **38**, 3098–3100.
- 40 C. Lee, W. Yang and R. G. Parr, *Phys. Rev. B: Condens. Matter Mater. Phys.*, 1988, **37**, 785–789.
- 41 M. Thomas, M. Brehm, R. Fligg, P. Vöhringer and B. Kirchner, *Phys. Chem. Chem. Phys.*, 2013, **15**, 6608–6622.
- 42 A. Bankura and A. Chandra, *Chem. Phys.*, 2012, **400**, 154–164.
- 43 T. Helgaker, W. Klopper, H. Koch and J. Noga, *J. Chem. Phys.*, 1997, **106**, 9639–9646.
- 44 T. Seki, K. Y. Chiang, C. C. Yu, X. Yu, M. Okuno, J. Hunger, Y. Nagata and M. Bonn, *J. Phys. Chem. Lett.*, 2020, **11**, 8459–8469.
- 45 D. J. Goebbert, E. Garand, T. Wende, R. Bergmann, G. Meijer, K. R. Asmis and D. M. Neumark, *J. Phys. Chem. A*, 2009, **113**, 7584–7592.
- 46 E. Garand, T. Wende, D. J. Goebbert, R. Bergmann, G. Meijer, D. M. Neumark and K. R. Asmis, *J. Am. Chem. Soc.*, 2010, **132**, 849–856.
- 47 E. Perl, M. von Domaros, B. Kirchner, R. Ludwig and F. Weinhold, *Sci. Rep.*, 2017, **7**, 1–10.
- 48 K. H. Lemke and T. M. Seward, *Rev. Min. Geochem.*, 2018, **84**, 57–83.